Energy & Environmental Science

ROYAL SOCIETY OF CHEMISTRY

COMMUNICATION

View Article Online
View Journal

Cite this: DOI: 10.1039/d6ee00100a

Received 7th January 2026,
Accepted 18th May 2026

DOI: 10.1039/d6ee00100a

rsc.li/ees

Hydrogen-free exsolution of Ir–Fe nanoalloys on the surface of solid oxide cell perovskite air electrodes

Jiyoon Shin,†[ab] Myung-Jin Jung,†[c] Hao-Yang Li,[b] Yujie Wu,[a] Wanwisa Limphirat,[d] Se-Hun Kwon *[c] and Pei-Chen Su *[ab]

Metal nanoparticle decoration *via* exsolution in a hydrogen reducing environment has emerged as a powerful strategy to enhance the performance of solid oxide cell (SOC) perovskite air electrodes. The exsolution process is fundamentally constrained by its reliance on a reducing atmosphere (H_2), which is inherently incompatible with oxidizing conditions of air electrodes, thereby constraining the range of elements and systems that can be practically implemented. Here, we report a hydrogen-free exsolution pathway that directly forms stable, socketed nanoalloys in air. By harnessing the intrinsic chemical affinity and broad miscibility between iridium and iron, we demonstrate that atomic-layer-deposited Ir nanoparticles act as thermodynamic sinks, selectively redistributing Fe from $Sr_2Fe_{1.5}Mo_{0.5}O_{6-\delta}$ (SFMO) perovskites during annealing in air. This process directly yields anchored Ir–Fe nanoalloys without the need for reducing gas. The Ir–Fe anchored SFMO electrodes exhibit improved activity and stability at 800 °C. The resulting socketed architecture not only resists coarsening but also mitigates surface strain, suppresses Sr segregation, and enhances oxygen exchange kinetics. This work establishes affinity-driven socketed nanoparticle formation as a distinct hydrogen-free exsolution pathway for SOC air electrodes.

Broader context

Metal surface decoration is a powerful strategy for enhancing the catalytic activity of solid oxide cell air electrodes, yet its practical impact is limited by the poor thermal stability of deposited nanoparticles under high-temperature oxidizing conditions. Exsolution offers a more robust solution by generating socketed nanoparticles that are anchored within the perovskite surface and resistant to coarsening or detachment. However, conventional exsolution relies on hydrogen reduction, which is intrinsically incompatible with the operating environment of air electrodes. This fundamental mismatch has restricted the practical use of exsolution for air–electrode surface engineering. Here, we establish a hydrogen-free exsolution pathway that directly forms socketed Ir–Fe nanoalloys in air. By harnessing the intrinsic alloy affinity between Ir and Fe, atomic-layer-deposited Ir nanoparticles act as thermodynamic sinks that selectively redistribute Fe from the $Sr_2Fe_{1.5}Mo_{0.5}O_{6-\delta}$ (SFMO) perovskite lattice during air annealing. This work demonstrates that alloy thermodynamics can replace external hydrogen reduction as the driving force for exsolution, providing an air-compatible design route toward stable catalytic surfaces for solid oxide cells.

1. Introduction

Solid oxide cells (SOCs) are promising electrochemical systems for high-efficiency energy conversion, but their air electrodes remain fundamentally limited by surface-related degradation.[1–5] At typical operating temperatures of 600–900 °C, perovskite air electrodes experience two main degradation pathways: (i) rapid coarsening or detachment of the electrode surface, and (ii) A-site cation (Sr^{2+} or Ba^{2+}) segregation toward the surface, forming insulating secondary phases that poison active sites for oxygen reduction and evolution reactions (ORR/OER).[6–9] These instabilities are widely recognized as the primary barrier to durable air electrode performance. To mitigate such degradation, many researchers have explored surface modification with metals such as Pt,[10] Pd,[11] Ag,[12–14] and Ru.[15,16] While these metal infiltrations initially improve oxygen reaction kinetics, the benefits are inherently transient: deposited nanoparticles readily agglomerate, volatilize, or detach at elevated temperatures (>450 °C).[17–19]

To combat these issues, exsolution has attracted strong interest as a more robust surface modification strategy, as exsolved nanoparticles are socketed within the perovskite backbone, offering resistance to coarsening.[19–21] However, conventional exsolution requires a strongly reducing atmosphere (typically H_2) to

[a] School of Mechanical and Aerospace Engineering, Nanyang Technological University, 50 Nanyang Avenue, 639798, Singapore. E-mail: peichensu@ntu.edu.sg
[b] Energy Research Institute@NTU (ERI@N), Interdisciplinary Graduate School, Nanyang Technological University, 50 Nanyang Drive, Singapore, 637553, Singapore
[c] School of Materials Science and Engineering, Pusan National University, Busan 46241, Republic of Korea. E-mail: sehun@pusan.ac.kr
[d] Synchrotron Light Research Institute (Public Organization), 111 University Avenue, Muang District, Nakhon Ratchasima 30000, Thailand
† J. Shin and M.-J. Jung contributed equally to this work.

create oxygen vacancies and mobilize B-site cations toward the surface.[22] This requirement makes exsolution essentially incompatible with air electrodes, which operate in a high-temperature oxidizing environment. Although several hydrogen-free exsolution-related strategies have been reported through A-site deficiency or steam-/water-mediated treatments in proton-conducting perovskites,[23–25] these approaches have been mainly demonstrated in PCFC applications, where water generated or supplied at the air electrode can actively participate in steam-/hydration-mediated surface reconstruction. This situation exposes a critical conceptual gap: the ability to trigger and stabilize catalytically active socketed nanoparticles directly in air, which is a real SOC air electrode condition, relying solely on inherent material chemistry without any external reducing step.

Addressing this gap demands a shift from external environments to an intrinsic chemical driving force. We speculate that the strategic selection of a surface-decorated metal with high chemical affinity and miscibility with a target B-site cation in the host perovskite can provide the requisite thermodynamic sink to drive exsolution, without the need for any reducing atmosphere. Herein, we demonstrate this principle using the model system of Ir on $Sr_2Fe_{1.5}Mo_{0.5}O_{6-\delta}$ (SFMO). Iridium exhibits a wide solid-solution range with iron,[26,27] making it a powerful thermodynamic sink for Fe. We show that Ir nanoparticles, deposited *via* atomic layer deposition (ALD), spontaneously extract Fe from the SFMO B-site lattice during high-temperature annealing in air, driven solely by the favorable energetics of Ir–Fe alloy formation.

This hydrogen-free exsolution mechanism leads to chemical affinity-driven, socketed Ir–Fe nanoalloys. This process confers multiple synergistic advantages: (1) the socketed geometry ensures nanoparticle stability against coarsening; (2) the incorporation of Fe into Ir modifies the surface electronic structure and relaxes elastic strain, which in turn suppresses the driving force for Sr segregation; and (3) the resulting nanoalloy surface enhances oxygen surface exchange and charge transfer kinetics. These effects produce air electrodes with improved and highly stable performance at 800 °C. More importantly, this work establishes alloy affinity as an effective chemical driving force for air-compatible exsolution-like surface reconstruction in Fe-containing perovskite air electrodes. By replacing external H_2 reduction with intrinsic alloy thermodynamics, this strategy opens a new route toward stable catalytic surfaces for next-generation reversible SOCs.

2. Results and discussion

2.1. Alloy-thermodynamics-driven exsolution in an oxidizing atmosphere

We demonstrate that the intrinsic chemical affinity between iridium and iron serves as a sufficient driving force to trigger metal exsolution directly in air, bypassing the need for a reducing atmosphere. This is conclusively evidenced by the evolution of socketed Ir–Fe nanoalloys on the $Sr_2Fe_{1.5}Mo_{0.5}O_{6-\delta}$ (SFMO) surface after annealing in air at 800 °C, a process schematically illustrated in Fig. 1. Unlike conventional reduction-driven exsolution, this pathway is initiated by atomic-layer-deposited Ir nanoparticles acting as thermodynamic sinks for Fe. The strong Ir–Fe miscibility selectively redistributes Fe from the surrounding SFMO matrix during annealing, leading to the formation of epitaxially anchored bimetallic particles. This result provides direct validation of our core hypothesis: alloy formation energetics can replace H_2 reduction as the primary driver of socketed nanoparticle emergence under oxidizing conditions.

The structural evolution from deposited Ir to socketed Ir–Fe alloys is captured by transmission electron microscopy (TEM) and spectroscopy (XPS and XAS). While bare SFMO shows a clean, unmodified perovskite surface (Fig. 2a), ALD delivers well-dispersed metallic Ir nanoparticles, with Ir (1 1 1) lattice fringes of 0.22 nm (Fig. 2b). STEM-EDX mapping of the as-deposited Ir/SFMO sample before air annealing shows Ir nanoparticles on the SFMO surface, while Fe remains primarily associated with the SFMO matrix (Fig. S1). This initial-state reference supports that local Ir–Fe co-enrichment develops during the subsequent air-annealing step. After 800 °C air annealing, a distinct transformation occurs: the Ir particles incorporate Fe that has migrated from the SFMO backbone, and the Ir–Fe nanoparticles become partially embedded within the perovskite surface, exhibiting the characteristic socketed morphology of exsolved particles (Fig. 2c and d). Crucially, energy-dispersive X-ray (EDX) mapping confirms the colocalization of Ir and Fe within these anchored nanoparticles, while Sr, Mo, and O signals remain homogeneously distributed in the bulk (Fig. 2d). We further performed STEM-EDX line-scan analyses across these Ir-containing nanoparticles (Fig. S2 and S3). These line profiles show local Fe enrichment accompanying Ir enrichment at the nanoparticle regions after annealing in air. This spatially resolved

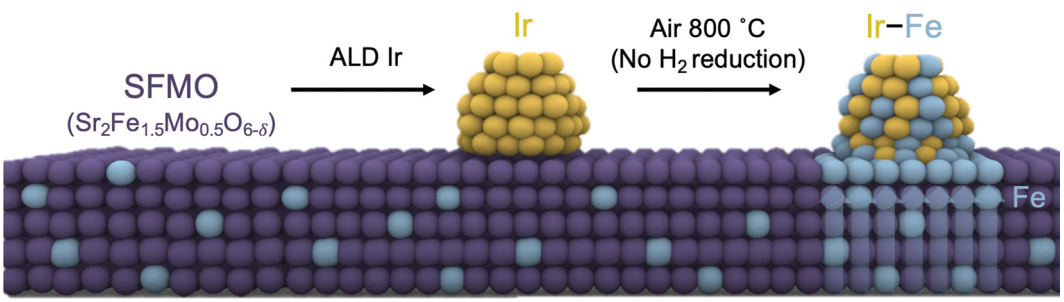

Fig. 1 Hydrogen-free Ir–Fe alloy formation on SFMO under oxidizing conditions. Schematic illustration of the Ir–Fe affinity-driven exsolution pathway. Ir nanoparticles deposited by ALD on SFMO act as seeds for a chemical affinity-driven process that, upon heating in air to 800 °C, pulls Fe cations from the perovskite lattice and forms socketed Ir–Fe nanoalloys without any reducing atmosphere.

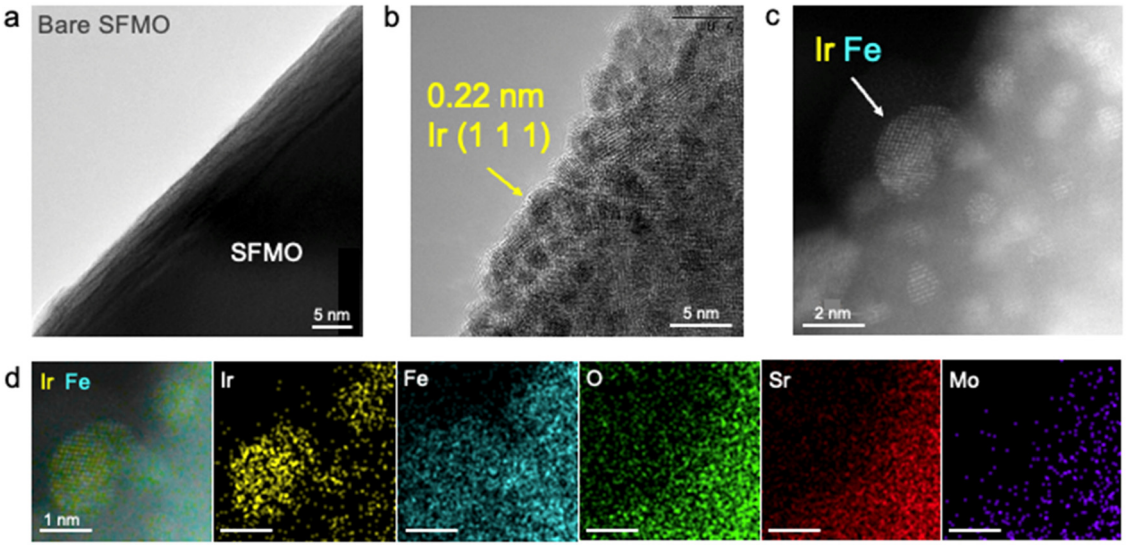

Fig. 2 Structural and compositional evolution of hydrogen-free Ir–Fe alloy formation on SFMO. TEM images of (a) bare SFMO, (b) Ir deposited on SFMO after ALD, and (c) Ir–Fe alloys embedded in the SFMO surface after annealing. (d) STEM-EDX maps of Ir–Fe nanoalloys on SFMO after annealing.

chemistry confirms that Fe has migrated from the SFMO lattice into the Ir nanoparticles, forming Ir–Fe nanoalloys without the presence of a reducing gas. Unlike infiltrated nanoparticles, which merely sit on the perovskite surface as unanchored deposits, the alloy particles are atomically anchored to the underlying SFMO lattice. This socketed geometry is key to the exsolution process and prevents particle coarsening or detachment at elevated temperature. Although Ir can partially oxidize at 800 °C in air, our EXAFS and STEM-EDX results confirm that Ir–Fe metallic coordination dominates the local structure of the resulting nanoparticles, indicating that alloy formation proceeds alongside or prior to complete oxidation.

2.2. Spectroscopic evidence of Fe exsolution and alloy formation

The mechanism of Fe redistribution and alloy formation is further corroborated by changes in the electronic and local coordination environments of Ir and Fe (Fig. 3). The Ir 4f spectrum of the as-ALD sample (Ir on SFMO, Fig. 3a) is dominated by metallic Ir^0 (79.6% of total Ir; binding energies of 61.2 eV and 64 eV), with a minor $Ir^{\delta+}$ component (20.4%) likely associated with interfacial Ir–O bonding with the SFMO oxide surface during the ALD process. After air annealing, the Ir 4f peaks shift positively by ~0.9 eV, and the $Ir^{\delta+}$ fraction increases to 52.5% (Fig. 3b). This shift is characteristic of charge redistribution upon Ir-based alloying, as reported for Ir–Co and Ir–Fe systems,[28–30] and confirms the electronic structure

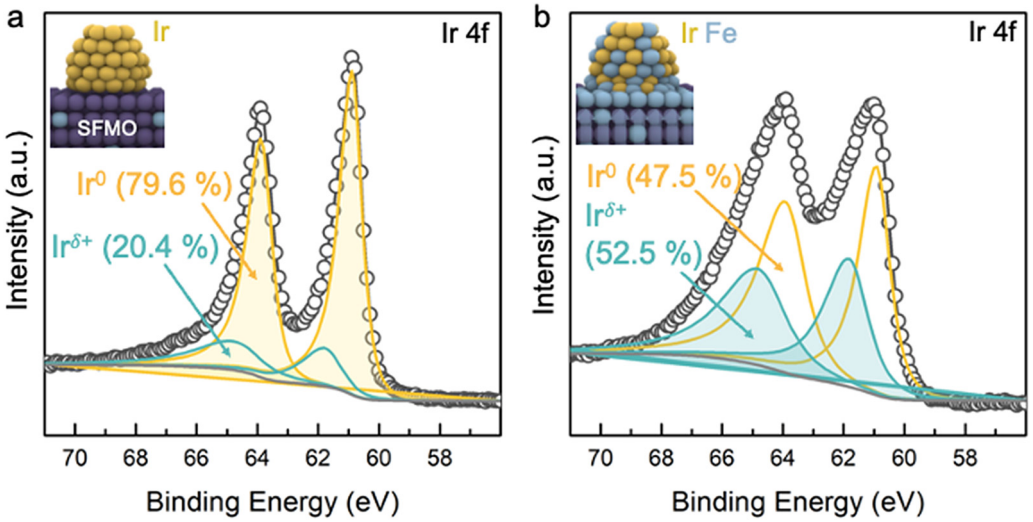

Fig. 3 Chemical affinity-driven Ir–Fe alloy formation on SFMO. (a) XPS Ir 4f spectrum of Ir on SFMO with a dominant metallic Ir component (Ir^0, 79.6%) and minor higher binding energy Ir species ($Ir^{\delta+}$, 20.4%), showing that ALD Ir nanoparticles are metallic on the as-prepared electrode surface. (b) XPS Ir 4f spectrum of Ir–Fe on SFMO after air annealing, showing an increase of the higher binding energy Ir fraction ($Ir^{\delta+}$, 52.5%) from Ir–Fe alloy formation under air annealing.

change in Ir due to Fe incorporation. The data rule out simple oxidation of Ir, reinforcing that the dominant process is Ir–Fe alloy formation.

Direct atomic-scale evidence comes from X-ray absorption spectroscopy (XAS). The Ir L_3-edge Fourier-transformed EXAFS spectrum of the annealed sample shows the emergence of new coordination paths at ~2.5 Å and ~3.7 Å, attributed to Ir–Fe first- and second-shell scattering, respectively,[31–33] alongside a weakened Ir–Ir contribution (Fig. 4a). Concurrently, Fe K-edge EXAFS reveals the appearance of a distinct Fe–Fe(Ir) metallic coordination peak at ~2.2 Å,[34,35] only in the Ir-decorated sample after annealing (Fig. 4b). This metallic Fe signature is absent in both the as-prepared sample and the annealed bare SFMO control. This contrast proves conclusively that Fe exsolution is not a spontaneous thermal process but is explicitly triggered by the presence of Ir. Together, these spectroscopic data provide a coherent picture of a surface reconstruction driven by Ir–Fe affinity, where Fe is drawn from the lattice into the waiting Ir nanoparticles to form a stable, metallic alloy under oxidizing conditions.

2.3. Electrochemical enhancement and surface stabilization

The electrochemical measurements were performed using a half-cell structure to isolate the air electrode polarization response under controlled oxidizing conditions. This configuration is appropriate for evaluating changes in air electrode oxygen exchange related impedance features while minimizing convolution from fuel electrode kinetics, fuel utilization, gas cross-effects, and full-cell engineering variables.[36,37] Therefore, the results are interpreted as comparative air electrode polarization behavior rather than full-cell device performance.

The hydrogen-free exsolved Ir–Fe nanoalloys deliver dual benefits: enhanced oxygen exchange kinetics and long-term stability, directly addressing the principal degradation pathways of SOC air electrodes. Electrochemical impedance spectroscopy (EIS) at 800 °C in air shows that the polarization resistance (R_p) of the Ir–Fe on the SFMO electrode is not only lower initially (0.53 Ω cm^2) than that of bare SFMO (0.60 Ω cm^2) but remains stable over 50 hours of operation (Fig. 5a and b). In stark contrast, bare SFMO suffers severe degradation, with R_p increasing by >50%, a phenomenon widely linked to progressive Sr surface segregation.

Distribution of relaxation times (DRT) analysis deconvolutes the source of this improvement. The intermediate-frequency (IF) and low-frequency (LF) processes,[38–41] associated with surface exchange and oxygen incorporation/diffusion, are suppressed for the Ir–Fe decorated electrode, while the high-frequency bulk response remains unchanged (Fig. 5c and Fig. S4). This indicates that the Ir–Fe nanoalloys specifically accelerate the surface oxygen exchange kinetics. More importantly, the near-constant R_p confirms that the socketed alloy nanoparticles effectively mitigate degradation.

We attribute this stability to two interconnected effects of the alloy exsolution process: (i) the socketed geometry of the nanoparticles inherently prevents coalescence and detachment, and (ii) the incorporation of Fe into the surface layer relaxes interfacial elastic strain, thereby reducing the thermodynamic driving force for Sr segregation. Thus, the Ir–Fe nanoalloys act as a self-stabilizing surface architecture, simultaneously enhancing and preserving electrochemical activity.

3. Conclusion

This work establishes a fundamentally different exsolution mechanism in which intrinsic Ir–Fe miscibility and alloy formation energetics, rather than hydrogen treatment, drive the emergence of socketed nanoparticles directly under oxidizing

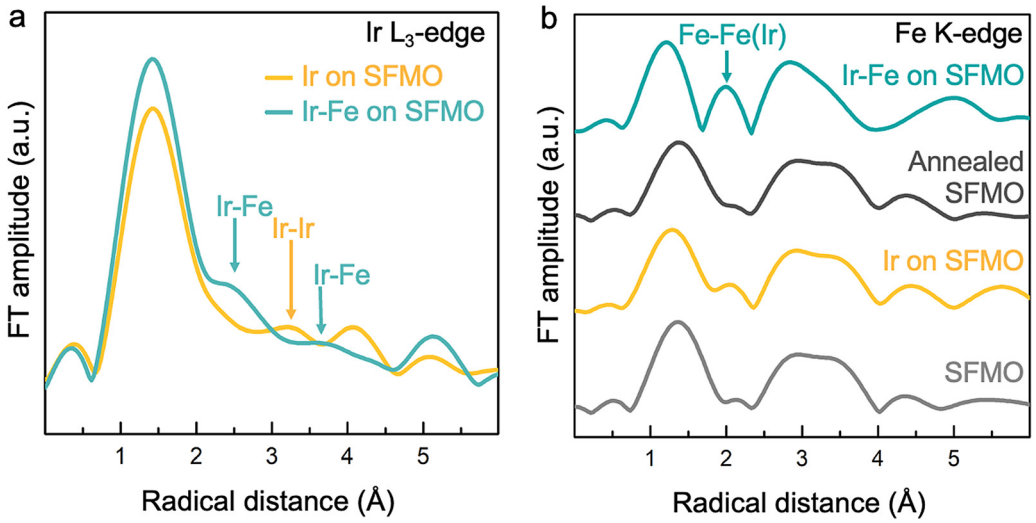

Fig. 4 Direct structural evidence of chemical affinity-driven Fe exsolution and Ir–Fe alloy formation on SFMO from EXAFS. (a) Fourier-transformed Ir L_3-edge EXAFS spectra of Ir on SFMO (yellow) and Ir–Fe on SFMO (blue) at room temperature. After air annealing, new coordination features appear at 2.5 Å (Ir–Fe first shell) and 3.7 Å (Ir–Fe second shell), while the Ir–Ir contribution is attenuated, confirming Ir–Fe alloy formation. (b) Fe K-edge EXAFS spectra before and after 800 °C annealing. Both Ir on SFMO (yellow) and bare SFMO (light grey) show weak Fe coordination before annealing, indicating Fe resides within the perovskite lattice. Ir–Fe on SFMO (blue) shows a new Fe–Fe metallic coordination peak (~2.2 Å), demonstrating Fe exsolution and alloying with Ir, whereas annealed bare SFMO (dark grey) remains unchanged, confirming that Fe exsolution is triggered by Ir–Fe affinity under oxidizing conditions.

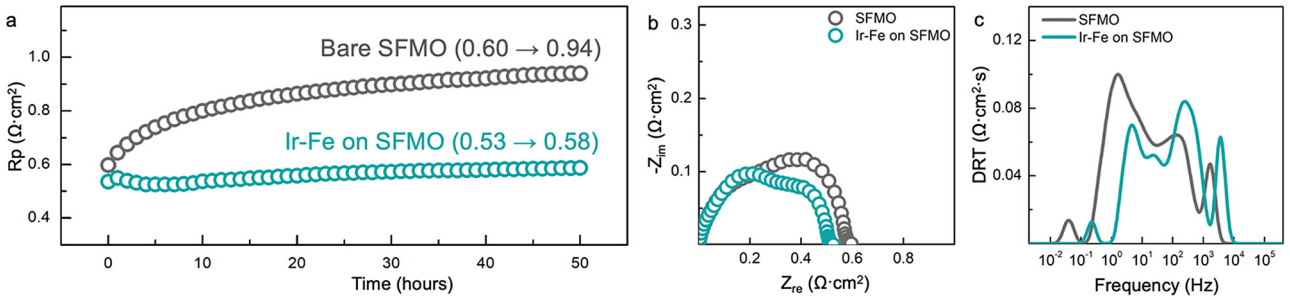

Fig. 5 Electrochemical impact of Ir–Fe alloy formation on SFMO air electrodes (800 °C in air). (a) Time evolution of polarization resistance (R_p) over 50 hours, showing severe degradation for bare SFMO and stable R_p for Ir–Fe on SFMO. (b) Nyquist plots and (c) distribution of relaxation times (DRT) spectra at the beginning of the test (0 h at 800 °C), showing improved surface charge-transfer and oxygen-exchange kinetics.

air. By selectively redistributing Fe from the surrounding SFMO matrix into Ir nanoparticles during 800 °C operation, our strategy enables hydrogen-free, air-compatible exsolution that reconstructs the surface, relaxes local strain, and suppresses Sr-driven surface degradation pathways. The resulting Ir–Fe nanoalloys simultaneously enhance the activity and stability of the air electrode, proving that exsolution-like surface reconstruction can be chemically promoted under oxidizing air electrode relevant conditions. This provides an alternative pathway for surface engineering of SOC air electrodes, avoiding the need for pre-reduction treatments. More broadly, the discovery introduces that alloy affinity can provide a useful design concept for promoting exsolution-like surface reconstruction in Fe-containing perovskites for air electrodes. This strategy advances a new design concept for hydrogen-free surface reconstruction in Fe-containing perovskite air electrodes and opens a promising route toward stable catalytic surface/interfaces for solid oxide cells.

Author contributions

J. Shin carried out the material synthesis, characterization, and electrochemical measurement. M.-J. Jung optimized the conditions for the deposition of iridium nanoparticles using atomic layer deposition. M.-J. Jung, H.-Y. Li, Y. Wu, and S.-H. Kwon provided constructive suggestions for material characterization and data analysis. W. Limphirat conducted synchrotron XAS analysis. J. Shin and P.-C. Su wrote the manuscript draft. All the authors contributed to the discussion and revision of the manuscript.

Conflicts of interest

The authors declare no conflicts of interest.

Data availability

The data supporting this article have been included as part of the supplementary information (SI). Supplementary information: experimental details and supporting datasets. See DOI: https://doi.org/10.1039/d6ee00100a.

Acknowledgements

The authors would like to acknowledge Dr Tay Yee Yan from the Facility for Analysis, Characterization, Testing and Simulation (FACTS), Nanyang Technological University (NTU), Singapore, for advice on the operation of electron microscopies. Additionally, the authors would like to thank FACTS at NTU, Singapore, for utilizing their electron microscopy and X-ray facilities. The project was supported by the National Research Foundation, Prime Minister's Office, Singapore, under its Campus for Research Excellence and Technological Enterprise (CREATE) program, as part of the Grand Challenge on Decarbonization with Ammonia Using SOFC for Power Generation. This work was also supported by NTU - JSPS Bilateral Joint Research Program Number JPJSBP120259003 between Japan and Singapore. This research was supported by the National Research Foundation of Korea (NRF) grant funded by the Korea government (MSIT) (No. RS-2024-00348696462182065300103).

References

1 D. Ding, X. Li, S. Y. Lai, K. Gerdes and M. Liu, *Energy Environ. Sci.*, 2014, **7**, 552–575.
2 H. Choi, J. Shin, C. Yeon, S.-Y. Park, S.-T. Bae, J. W. Kim, J.-H. Lee, J.-W. Park, C.-W. Lee and K. J. Yoon, *Energy Environ. Sci.*, 2024, **17**, 5410–5420.
3 L. Fan, B. Zhu, P.-C. Su and C. He, *Nano Energy*, 2018, **45**, 148–176.
4 H. G. Seo, A. Staerz, D. S. Kim, D. Klotz, C. Nicollet, M. Xu, J. M. LeBeau and H. L. Tuller, *Energy Environ. Sci.*, 2022, **15**, 4038–4047.
5 C. Peng, X. Han, S. Mabaleha, P. Kwong, Y. Zheng and X. Xu, *Energy Environ. Sci.*, 2025, **18**, 4555–4595.
6 J. Shin, H.-Y. Li, Y. Wu, K. Park, J. W. Shin, S. Wannapaiboon, W. Limphirat, J. An and P.-C. Su, *ACS Energy Lett.*, 2025, **11**(1), 782–789.
7 W. Feng, G. Zou, T. Liu, R. Li, J. Yu, Y. Guo, Q. Liu, X. Zhang, J. Wang and N. Ta, *Energy Environ. Sci.*, 2025, **18**, 2273–2284.
8 S. Koohfar, M. Ghasemi, T. Hafen, G. Dimitrakopoulos, D. Kim, J. Pike, S. Elangovan, E. D. Gomez and B. Yildiz, *Nat. Commun.*, 2023, **14**, 7203.

9 W. Jung and H. L. Tuller, *Energy Environ. Sci.*, 2012, **5**, 5370–5378.
10 H. Uchida, *Solid State Ionics*, 2000, **135**, 347–351.
11 F. Liang, J. Chen, S. P. Jiang, B. Chi, J. Pu and L. Jian, *Electrochem. Commun.*, 2009, **11**, 1048–1051.
12 K. T. Lee and A. Manthiram, *J. Power Sources*, 2006, **160**, 903–908.
13 Y. Sakito, A. Hirano, N. Imanishi, Y. Takeda, O. Yamamoto and Y. Liu, *J. Power Sources*, 2008, **182**, 476–481.
14 C.-C. Yu, J. D. Baek, C.-H. Su, L. Fan, J. Wei, Y.-C. Liao and P.-C. Su, *ACS Appl. Mater. Interfaces*, 2016, **8**, 10343–10349.
15 H. A. Ishfaq, S. U. Rehman, M. Z. Khan, T. Sattar, M. Saleem, J.-H. Koh, I. Hussain, A. Hussain, S. Qamar and A. Ghaffar, *ACS Appl. Energy Mater.*, 2025, **8**, 15069–15078.
16 J. Wang, J. Zhou, J. Yang, D. Neagu, L. Fu, Z. Lian, T. H. Shin and K. Wu, *Adv. Mater. Interfaces*, 2020, **7**(23), 2000828.
17 J. Shin, K. Kamlungsua, H.-Y. Li and P.-C. Su, *Int. J. Precision Eng. Manuf. Green Technol.*, 2024, **11**, 1207–1216.
18 K.-Y. Liu, L. Fan, C.-C. Yu and P.-C. Su, *Electrochem. Commun.*, 2015, **56**, 65–69.
19 C.-C. Yu, S. Kim, J. D. Baek, Y. Li, P.-C. Su and T.-S. Kim, *ACS Appl. Mater. Interfaces*, 2015, **7**, 6036–6040.
20 D. Neagu, J. T. Irvine, J. Wang, B. Yildiz, A. K. Opitz, J. Fleig, Y. Wang, J. Liu, L. Shen and F. Ciucci, *J. Phys. Energy*, 2023, **5**, 031501.
21 Y. Song, Y. Song, Y. Wang, Y. Tian, J. Li, M. Xu, Z. Shao and F. Ciucci, *Adv. Funct. Mater.*, 2024, **34**, 2405851.
22 Z. Liu, L. Zhang, C. J. Zheng, Y. Zhang, B. Chen, Z. Shao and J. Ge, *Adv. Mater.*, 2025, **37**(48), 2503609.
23 K. Park, M. Saqib, H. Lee, D. Shin, M. Jo, K. M. Park, M. Hamayun, S. H. Kim, S. Kim and K.-S. Lee, *Energy Environ. Sci.*, 2024, **17**, 1175–1188.
24 J. H. Kim, J. Hong, D.-K. Lim, S. Ahn, J. Kim, J. K. Kim, D. Oh, S. Jeon, S.-J. Song and W. Jung, *Energy Environ. Sci.*, 2022, **15**, 1097–1105.
25 M. Liang, Y. Zhu, Y. Song, D. Guan, Z. Luo, G. Yang, S. P. Jiang, W. Zhou, R. Ran and Z. Shao, *Adv. Mater.*, 2022, **34**, 2106379.
26 L. J. Cabri and T. Aiglsperger, *Mineral. Mag.*, 2018, **82**, 531–538.
27 X. Yang, Y. Li, L. Deng, W. Li, Z. Ren, M. Yang, X. Yang and Y. Zhu, *RSC Adv.*, 2017, **7**, 20252–20258.
28 X. Liu, S. Xi, H. Kim, A. Kumar, J. Lee, J. Wang, N. Q. Tran, T. Yang, X. Shao and M. Liang, *Nat. Commun.*, 2021, **12**, 5676.
29 X. Cao, H. Cheng, R. Gui, H. Zhang, C. Su, C. Chen, Y. Yin, Y. Tan, H. Wang and W. Chu, *Angew. Chem.*, 2025, **137**, e202509993.
30 A. L. Maulana, P.-C. Chen, Z. Shi, Y. Yang, C. Lizandara-Pueyo, F. Seeler, H. D. Abruña, D. Muller, K. Schierle-Arndt and P. Yang, *Nano Lett.*, 2023, **23**, 6637–6644.
31 S. Czioska, A. Boubnov, D. Escalera-López, J. Geppert, A. Zagalskaya, P. Röse, E. Saraçi, V. Alexandrov, U. Krewer and S. Cherevko, *ACS Catal.*, 2021, **11**, 10043–10057.
32 J. Zhao, Y. Guo, Z. Zhang, X. Zhang, Q. Ji, H. Zhang, Z. Song, D. Liu, J. Zeng and C. Chuang, *Nat. Nanotechnol.*, 2025, **20**, 57–66.
33 Q. Wang, C.-Q. Xu, W. Liu, S.-F. Hung, H. Bin Yang, J. Gao, W. Cai, H. M. Chen, J. Li and B. Liu, *Nat. Commun.*, 2020, **11**, 4246.
34 J. Timoshenko and B. Roldan Cuenya, *Chem. Rev.*, 2020, **121**, 882–961.
35 F. X. Zhang, K. Jin, S. Zhao, S. Mu, H. Bei, J. C. Liu, H. Z. Xue, D. Popov, C. Park and G. M. Stocks, *J. Appl. Phys.*, 2017, **121**(16), 165105.
36 J. C. Ruiz-Morales, D. Marrero-López, J. Canales-Vázquez and J. T. Irvine, *RSC Adv.*, 2011, **1**, 1403–1414.
37 S. Kim, S. Lee, J. Kim, J. Shin and G. Kim, *Sci. Rep.*, 2018, **8**, 17149.
38 A. C. Lazanas and M. I. Prodromidis, *ACS Meas. Sci. Au*, 2023, **3**, 162–193.
39 Z. L. M. Botello, A. Montenegro-Hernández, L. Mogni and G. H. Gauthier, *Electrochim. Acta*, 2021, **365**, 137332.
40 C. Riedl, M. u Siebenhofer, A. Nenning, G. E. Wilson, J. Kilner, C. Rameshan, A. Limbeck, A. K. Opitz, M. Kubicek and J. Fleig, *ACS Appl. Mater. Interfaces*, 2023, **15**, 26787–26798.
41 Z. Zheng, J. Jing, Z. Lei, Z. Wang, Z. Yang, C. Jin and S. Peng, *Int. J. Hydrogen Energy*, 2022, **47**, 18139–18147.

